





On the Superconductivity Suppression in $\text{Eu}_{1-x}\text{Pr}_x\text{Ba}_2\text{Cu}_3\text{O}_{7-\delta}$

Paweł Pęczkowski ^{1,*} , Piotr Zachariasz ² , Cezariusz Jastrzębski ³ , Jarosław Piętosa ⁴, Elżbieta Drzymała ⁵ and Łukasz Gondek ⁶ 

- ¹ Institute of Physical Sciences, Faculty of Mathematics and Natural Sciences, School of Exact Sciences, Cardinal Stefan Wyszyński University, K. Wóycickiego 1/3 Street, 01-938 Warsaw, Poland
 - ² LTCC Technology and Printed Electronics Research Group, Łukasiewicz Research Network—Institute of Microelectronics and Photonics, Zabłocie 39 Street, 30-701 Kraków, Poland; piotr.zachariasz@imif.lukasiewicz.gov.pl
 - ³ Faculty of Physics, Warsaw University of Technology, Koszykowa 75 Street, 00-662 Warsaw, Poland; cezjas@gmail.com
 - ⁴ Group of Phase Transition, Division of Physics of Magnetism, Institute of Physics, Polish Academy of Sciences, Lotników 32/46 Avenue, 02-668 Warsaw, Poland; pietosa@ifpan.edu.pl
 - ⁵ Department for Functional Nanomaterials, The Henryk Niewodniczański Institute of Nuclear Physics, Polish Academy of Sciences, W.E. Radzikowskiego 152 Street, 31-342 Kraków, Poland; elzbieta.drzymala@ifj.edu.pl
 - ⁶ Department of Solid State Physics, Faculty of Physics and Applied Computer Science, AGH University of Science and Technology, A. Mickiewicza 30 Avenue, 30-059 Kraków, Poland; lgondek@agh.edu.pl
- * Correspondence: p.peczkowski@wp.pl or p.peczkowski@uksw.edu.pl

Abstract: This article reports on the non-trivial suppression of superconductivity in the $\text{Eu}_{1-x}\text{Pr}_x\text{BCO}$ cuprates. As non-magnetic Eu^{3+} ions are replaced by Pr^{3+} carrying a magnetic moment, spin-related superconductivity loss can be expected. The research shows that the superconductivity disappearance for $x > 0.4$ results from depletion of the carriers and their localization. The above conclusion was drawn by low-temperature X-ray diffraction analysis showing increased characteristic phonon frequencies with Pr content. This mechanism should promote electron–phonon coupling, at least for acoustic phonons. However, the inverse phenomenon was detected. Namely, there is a gradual deterioration of the optical phonons responsible for vibration of the Cu–O bonds with Pr increasing, as evidenced by Raman spectroscopy. Furthermore, the results of X-ray absorption spectroscopy precisely showed the location of the carriers for Pr-rich specimens. Finally, a schematic diagram for $\text{Eu}_{1-x}\text{Pr}_x\text{BCO}$ is proposed to consolidate the presented research.

Keywords: high-temperature superconductors; solid-state reaction method; magnetism; X-ray diffraction; Raman spectroscopy; X-ray absorption spectroscopy



Citation: Pęczkowski, P.; Zachariasz, P.; Jastrzębski, C.; Piętosa, J.; Drzymała, E.; Gondek, L. On the Superconductivity Suppression in $\text{Eu}_{1-x}\text{Pr}_x\text{Ba}_2\text{Cu}_3\text{O}_{7-\delta}$. *Materials* **2021**, *14*, 3503. <https://doi.org/10.3390/ma14133503>

Academic Editor: Dinesh Agrawal

Received: 23 April 2021

Accepted: 16 June 2021

Published: 23 June 2021

Publisher's Note: MDPI stays neutral with regard to jurisdictional claims in published maps and institutional affiliations.



Copyright: © 2021 by the authors. Licensee MDPI, Basel, Switzerland. This article is an open access article distributed under the terms and conditions of the Creative Commons Attribution (CC BY) license (<https://creativecommons.org/licenses/by/4.0/>).

1. Introduction

In 1986, Bednorz and Müller discovered the high-temperature superconductivity (HTS) in La-Ba-Cu-O , and the following year, they received the Nobel Prize in Physics, which indicates the incredible significance of this discovery for the energy and space industries, as well as for numerous technical and medical applications. The last point concerns, i.e., the superconducting magnets, SQUID-based devices, superconducting JJ-arrays (Josephson junctions), fault-current limiters, or magnetic levitation transport systems. Finally, the possibility to measure weak magnetic fields has released a wide range of biomedical applications (e.g., magnetoencephalography).

Historically, La-Ba-Cu-O was the first high-temperature superconductor (HTS) with a critical temperature (T_c) close to 36 K [1]. Later, by applying hydrostatic pressure, Chu [2] increased the superconducting state of $\text{La}_{5-x}\text{Ba}_x\text{Cu}_5\text{O}_{5(3-y)}$ up to 50 K, showing in practice that various conditions can effectively affect T_c .

In turn, a significant rise in critical temperature was observed for the REBa₂Cu₃O_{7-δ} family (RE—rare earth element); e.g., Wu and Chu [3] proved the oxygen-dependent $T_c \approx 90$ K for YBa₂Cu₃O_{7-δ}. Further studies of other rare earth elements [4–11] show that T_c can be even above 90 K for most RE³⁺ ions, despite possessing a spin magnetic moment, which is typically antagonistic for the superconducting state.

Nevertheless, there are a few exclusions to this rule. CeBa₂Cu₃O_{7-δ} and TbBa₂Cu₃O_{7-δ} [12] principally do not crystalize in the superconducting orthorhombic structure (*Pmmm*, No. 47; so-called RE-123 phase). In turn, PrBa₂Cu₃O_{7-δ} crystallizes in the orthorhombic Pr-123 structure; however, the superconductivity of bulk samples is rarely reported, which is presumably due to the Pr/Ba mixing being difficult to avoid [13–15].

As predicted theoretically, PrBa₂Cu₃O_{7-δ} shows superconductivity at $T_c \approx 90$ K with 90% ÷ 10% transition width of $\Delta T \approx 20$ K or less [16]. This behavior has been confirmed by studies on the superconductivity of thin layers [17], single crystals [18–20], and excellent polycrystalline samples [21]. However, the latter materials are challenging to synthesize since Pr-based ceramics are sensitive to sintering conditions, promoting the Pr/Ba exchange in the crystal structure [15,21]. Furthermore, since the interplanar bonds in cuprates are mainly ionic, the difference in radii Pr³⁺ (113.0 pm) and Ba²⁺ (149.0 pm) impacts the *c* lattice parameter of the *Pmmm* structure. In general, the *c* lattice constant for non-superconducting material is smaller than for the superconducting one [21].

Many researchers investigated the Y_{1-x}Pr_xBa₂Cu₃O_{7-δ} [22–24] and Gd_{1-x}Pr_xBa₂Cu₃O_{7-δ} systems [25] and found that the critical temperature (T_c) decreased monotonically with Pr concentration, similar to YBa₂Cu₃O_{7-δ}–YMnO₃ composites enriched with YMnO₃ [26].

NdBa₂Cu₃O_{7-δ} is a familiar system where Ba²⁺ can substitute Nd³⁺. However, the formation of Nd–Ba defects is much less frequent than the development of Pr–Ba defects [27]. The T_c variability can be explained by the Nd/Ba mixing frequency controlling the charge transfer from Cu–O₂ planes to Cu–O chains [27].

Research on the Eu_{1-x}Pr_xBa₂Cu₃O_{7-δ} system (regularly called (Eu,Pr)BCO or (Eu,Pr)-123 phase) was initiated in 1990, focusing on Mössbauer ¹⁵¹Eu spectroscopy and superconductivity suppression by Pr⁴⁺ ions at $x = 0.4$ [28]. In addition, research on specific heat has also been reported [29], where Pr contribution in the metallic phase is manifested by a broad anomaly quite well described by the Kondo method. Then, the entropy correlated with Pr anomalies in metallic and insulating phases indicates a twofold ground state of Pr with a valence close to 4⁺ in the crystalline electric field.

This paper aims to explain the non-trivial suppression of superconductivity in the (Eu_{1-x}Pr_x)BCO system ($x = 0.0; 0.2; 0.4; 0.6; 0.8; 1.0$). For the Eu³⁺ ion (4f⁶5s²5p⁶), the orbital and spin contributions in the total angular momentum (*J*) cancel each other, making the Eu-123 phase unique ($J = 0$). On the other hand, the Pr³⁺ ion (4f²5s²5p⁶) reveals $J = 4$. However, it is widely accepted that the ground state of the Pr³⁺ multiplet is an intrinsically non-magnetic singlet in a crystal electric field. Thus, superconductivity suppression in this particular case does not seem to be biased by magnetism.

2. Materials and Methods

2.1. Preparation of (Eu,Pr)BCO by Solid-State Reaction Method

Eu₂O₃, Pr₂O₃ (Sigma-Aldrich, St. Louis, MO, USA, 99.99% purity), CuO (Alfa-Aesar, Haverhill, MA, USA, 99.999% purity), and BaCO₃ (POCH, Gliwice, Poland, 99.6% purity) were used to prepare the Eu_{1-x}Pr_xBCO samples. First, the materials were synthesized by a conventional solid-state reaction method by calcining the stoichiometric weighed substrates at 950 °C for 24 h. Then, the sinters were crushed, ground, and calcination was repeated. Next, sintered materials were ground again and pelletized under a uniaxial pressure of 800 MPa. Finally, the pellets were annealed in an oxygen flow of 20 L/h at 920 °C. After 33 h, the temperature was lowered to 400 °C and held for the next 33 h, as described [8,9,30].

2.2. Characterization of Materials

Scanning Electron Microscopy (SEM) with Energy-Dispersive X-Ray Spectroscopy (EDS) was performed on the TESCAN VEGA 3 SBH instrument. The local microstructures were imaged using the SE detector in a high vacuum mode and at a voltage of 30 kV. The EDS detector equipped with the Bruker Esprit software analyzed the chemical compositions of (Eu,Pr)BCO. The SEM/EDS studies were conducted on fractured as well as on polished surfaces of pellets.

X-Ray Diffraction (XRD) studies were performed using the Empyrean PANalytical instrument operating in the Bragg–Brentano geometry with Cu K_{α} radiation ($\lambda = 1.5406 \text{ \AA}$) and NIST LaB₆ standard for correcting the instrument broadening. Diffractograms were collected over an angular range of $5^{\circ} < 2\theta < 130^{\circ}$. Low-temperature studies (15 ÷ 300 K) were made using Oxford Instruments. The specimen position was corrected against thermal displacements. The Rietveld analysis was employed [31,32] to quantify the diffraction patterns of (Eu,Pr)BCO.

Raman vibrational spectra were measured with the Renishaw micro-Raman inVia Reflex instrument in backscattering geometry. A 514 nm line of an Ar-ion laser with a spot diameter of about 1.5 μm was used to excite the material. The laser power has been adjusted so that the cumulative energy dose per sample did not exceed 1 mW to avoid laser-induced degradation effects. Raman spectra were collected cumulatively over three passes each for 30 s to enhance the signal-to-noise ratio.

X-ray absorption spectroscopy (XAS) was employed to inspect the (Eu,Pr)BCO electronic structure. The XAS data were recorded in a total-electron-yield mode from the area of $0.5 \times 0.3 \text{ mm}^2$ with a spectral resolution $\Delta E/E$ of $2.5 \cdot 10^{-4}$ and normalized for background calibration measurements. The research was carried out at the SOLARIS National Synchrotron Radiation Centre (Kraków, Poland) on the PEEM/XAS line. The experiment was accomplished in cooperation with the SOLARIS Staff.

Magnetic measurements as a function of temperature (5 ÷ 120 K) and magnetic field up to 50 kOe were carried out with a superconducting quantum interference magnetometer (Quantum Design, San Diego, CA, USA, MPMS-5).

The method of fixed-point titration with sodium thiosulfate ($\text{Na}_2\text{S}_2\text{O}_3$) was utilized to determine the oxygen concentration [33].

3. Results

3.1. Microstructural Analysis

The local microstructure evolution of the (Eu,Pr)BCO system is presented in Figure 1.

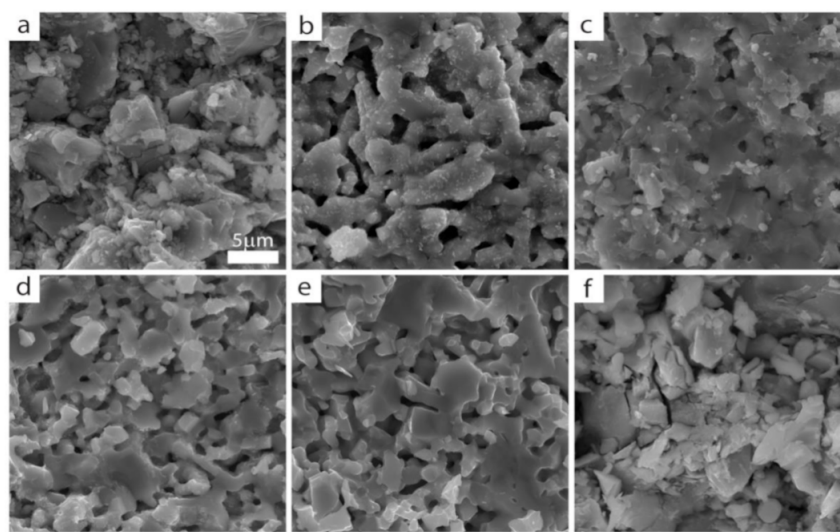


Figure 1. Scanning electron microscopy (SEM) images of the local microstructures: (a) EuBCO, (b) $\text{Eu}_{0.2}\text{Pr}_{0.8}\text{BCO}$, (c) $\text{Eu}_{0.4}\text{Pr}_{0.6}\text{BCO}$, (d) $\text{Eu}_{0.6}\text{Pr}_{0.4}\text{BCO}$, (e) $\text{Eu}_{0.8}\text{Pr}_{0.2}\text{BCO}$, and (f) PrBCO.

Comparable morphologies can be observed for all $\text{Eu}_{1-x}\text{Pr}_x\text{BCO}$ (Figure 1b–e), which are essentially different from the parent EuBCO and PrBCO . The latter compounds are characterized by distinct grains with sharp edges and sizes from 5 to 10 μm (for PrBCO even up to 15 μm).

In contrast, the $(\text{Eu},\text{Pr})\text{BCO}$ crystallites are finer and show more rounded edges, and it could even be said that the local microstructures of $(\text{Eu},\text{Pr})\text{BCO}$ are slightly glassy. The grain sizes rarely exceed 5 μm , and for $\text{Eu}_{0.2}\text{Pr}_{0.8}\text{BCO}$ (Figure 1b), one can find the delicate crystallites that decorate the surfaces of larger ones. In turn, $\text{Eu}_{0.4}\text{Pr}_{0.6}\text{BCO}$ (Figure 1c) has the most compact local microstructure of the other compounds.

Energy-dispersive X-ray spectroscopy was also employed to evaluate the contribution of individual elements (EDS mapping) in the $(\text{Eu},\text{Pr})\text{BCO}$ system (Figure 2).

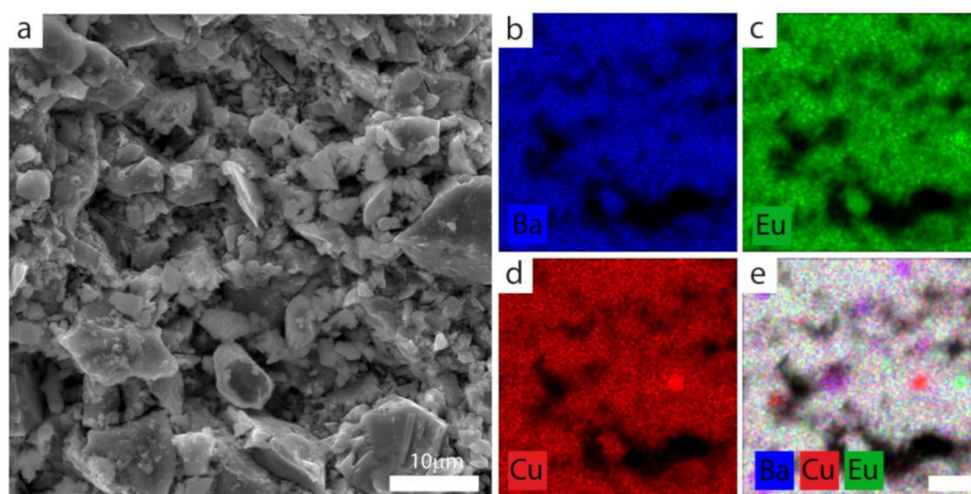


Figure 2. (a) Local microstructure (SEM) of EuBCO with EDS elemental maps showing the distribution of (b) Ba; (c) Eu; (d) Cu; (e) their overlapping.

Note that the EDS technique is a local estimation method and does not provide the average information from a bulk sample. However, as shown in Figure 2b–d, uniformly distributed elements in local microstructures develop small inclusion aggregates (Figure 2e).

Taking into account the constituent atoms—barium (blue), europium (green), copper (red)—and the RGB color model, one can estimate the chemical composition of the colored clusters detected by the EDS mapping technique. Then, the magenta aggregates (Figure 2e) should be attributed to the BaCuO_2 inclusions, the small greenish spots mark the $\text{Eu}_2\text{BaCuO}_5$ (Eu-211) parasitic phase, and red clusters understandably represent the residual CuO phase. Other $(\text{Eu},\text{Pr})\text{BCO}$ exhibit similar behavior, meaning that all specimens possess small although detectable inclusions.

Mainly red inclusions are visible for $(\text{Eu},\text{Pr})\text{BCO}$, indicating the CuO phase (Figure 3c). After overlapping the maps of the individual elements, the blue precipitations were found (Figure 3f). The specimens mentioned above show neither europium nor praseodymium clusters. As seen in the EDS maps for $\text{Eu}_{0.6}\text{Pr}_{0.4}\text{BCO}$ (Figure 3d,e), the Pr and Eu elements are homogeneously distributed. In order to estimate the stoichiometry on the macro scale, several regions of interest (ROIs) of $60 \times 60 \mu\text{m}^2$ were discriminated for each specimen, and the EDS mapping results are averaged and listed in Table 1.

Table 1. Stoichiometry of Eu and Pr as derived from EDS for $\text{Eu}_{1-x}\text{Pr}_x\text{BCO}$ compounds. Presented results aggregate several randomly selected areas with dimensions of $60 \times 60 \mu\text{m}^2$ (equivalent to the total area in Figure 2a).

Stoichiometric Parameter	$\text{Eu}_{0.8}\text{Pr}_{0.2}\text{BCO}$	$\text{Eu}_{0.6}\text{Pr}_{0.4}\text{BCO}$	$\text{Eu}_{0.4}\text{Pr}_{0.6}\text{BCO}$	$\text{Eu}_{0.2}\text{Pr}_{0.8}\text{BCO}$
x	0.20 ± 0.04	0.43 ± 0.06	0.64 ± 0.07	0.82 ± 0.06

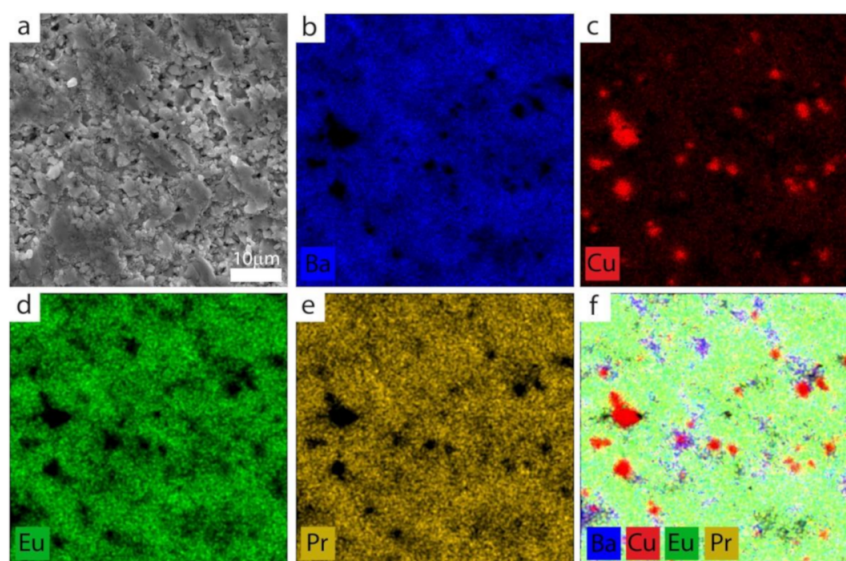


Figure 3. (a) Local microstructure (SEM) of $\text{Eu}_{0.6}\text{Pr}_{0.4}\text{BCO}$ with the corresponding EDS elemental maps showing the distribution of (b) Ba; (c) Cu; (d) Eu; (e) Pr; and (f) their overlapping.

During the synthesis of (Eu,Pr)BCO materials, the main concerns were maintaining the correct Pr/Eu ratio and the homogeneity of Pr and Eu. Indeed, EDS studies revealed that the Pr/Eu ratio is preserved in specimens. Moreover, relevant ROIs analysis completed on polished specimens (not shown here) with the assumed uncertainty level yielded the exact stoichiometry of EDS mapping.

3.2. X-ray Diffraction Analysis

According to structural refinement data (Table 2), the dominant phase in (Eu,Pr)BCO was indexed as the orthorhombic $Pmmm$ space group. An exemplary diffraction pattern for $\text{Eu}_{0.4}\text{Pr}_{0.6}\text{BCO}$ with Rietveld analysis is presented in Figure 4. The X-ray data refinement is of good quality with impurity phases less than 14 wt% of the sample. A similar level of impurities was detected for $\text{Eu}_{0.2}\text{Pr}_{0.8}\text{BCO}$, while for other composites, the total contribution of parasitic phases was below 5 wt%. A comparison of the collected X-ray patterns for (Eu,Pr)BCO is presented in Figure 5.

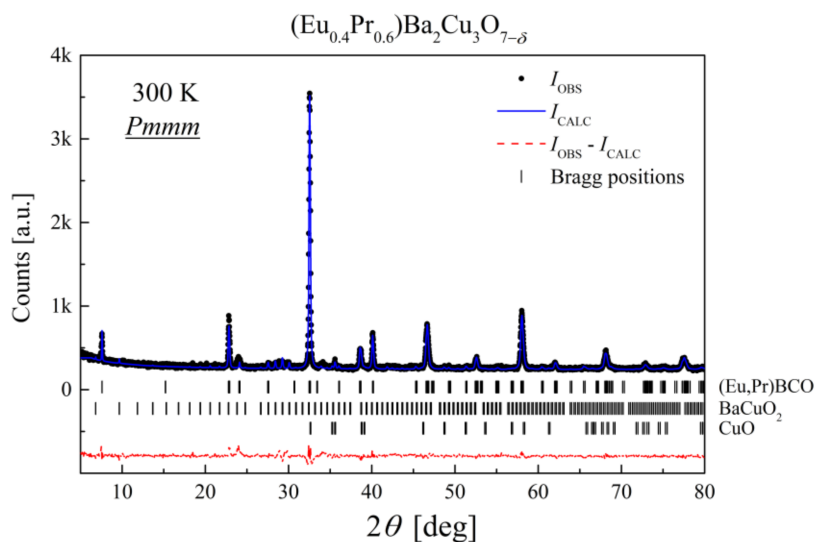
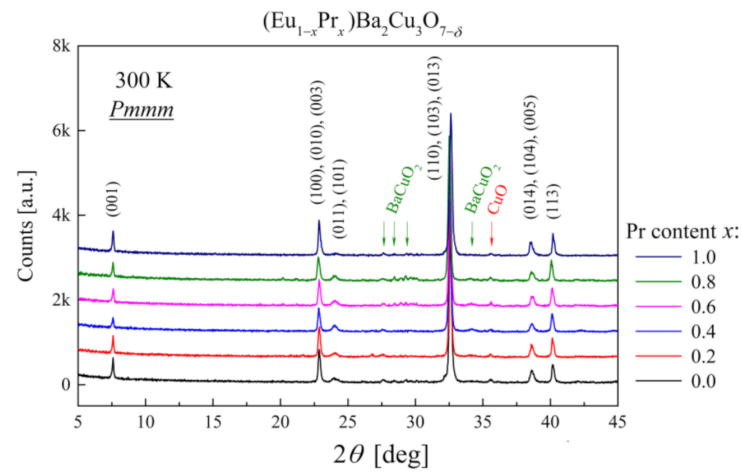


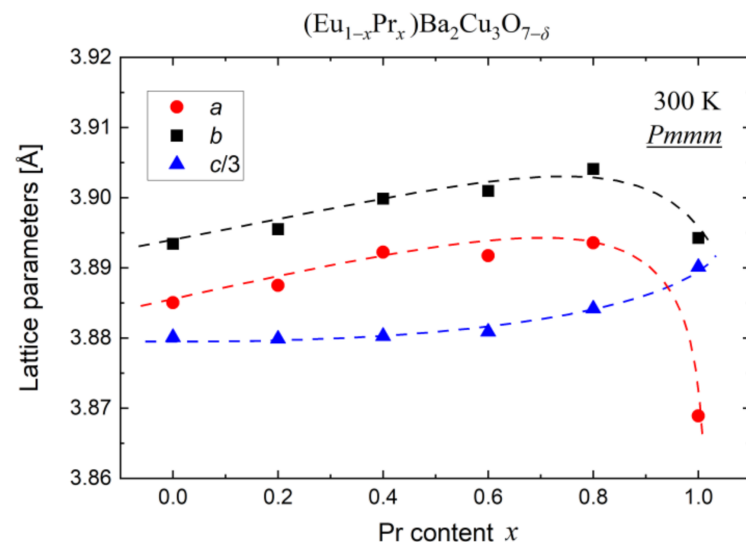
Figure 4. X-ray diffraction pattern of $\text{Eu}_{0.4}\text{Pr}_{0.6}\text{BCO}$. The isolated phases (Eu,Pr)BCO ($Pmmm$), BaCuO_2 , and CuO marked with bars are shown in descending order of their contributions.

Table 2. Weight fractions of isolated crystalline phases for (Eu,Pr)BCO as derived from Rietveld analysis.

Compound	(Eu,Pr)BCO [wt%]	BaCuO ₂ [wt%]	CuO [wt%]
EuBCO	96.0 ± 0.9	2.0 ± 0.2	2.0 ± 0.2
Eu _{0.8} Pr _{0.2} BCO	88.6 ± 0.9	4.2 ± 0.2	7.2 ± 0.3
Eu _{0.6} Pr _{0.4} BCO	92.1 ± 0.9	1.9 ± 0.2	6.0 ± 0.3
Eu _{0.4} Pr _{0.6} BCO	83.7 ± 0.7	8.2 ± 0.3	8.1 ± 0.4
Eu _{0.2} Pr _{0.8} BCO	83.4 ± 0.8	9.2 ± 0.5	7.4 ± 0.3
PrBCO	95.0 ± 0.9	2.0 ± 0.2	3.0 ± 0.2

**Figure 5.** Comparison of the X-ray diffraction patterns for (Eu,Pr)BCO. The parasitic phases are marked with arrows.

As shown in Figure 5, the PrBCO diffraction pattern exhibits some shifts of the Bragg reflections toward the lower 2θ angles compared to other samples. Indeed, analysis of the lattice parameters a and b suggests that PrBCO is the most oxygen-deficient material due to a significantly reduced unit cell volume. As other (Eu,Pr)BCO materials reveal a regular rise in lattice parameters (Figure 6) due to the lanthanide contraction principle [34,35], it would be expected that substituting Pr for Eu should increase the Pmmm unit cell volume. This effect is directly observed, although only up to $x \leq 0.8$.

**Figure 6.** The lattice parameters of (Eu,Pr)BCO distilled at room temperature.

On the other hand, the oxygen impact on the $Pmmm$ unit cell size is also known. In the orthorhombic phase, the parameters a and c decrease with increasing oxygen content [36]. Considering both effects, the rather monotonic growth in lattice parameters (Figure 6) indicates a similar oxygen content for all compounds except for PrBCO. Interestingly, the (Eu,Pr)BCO composition has almost no effect on the lattice parameter (c) to $x \leq 0.6$, reflecting the high structural anisotropy of these compounds.

As the ionic and covalent radii of Pr^{3+} are greater than Eu^{3+} , $\text{Eu}_{0.4}\text{Pr}_{0.6}\text{BCO}$ should be expected to have smaller lattice parameters than PrBCO. However, the unit cell volume is smaller for the latter compound, which is attributed to the oxygen deficiency in PrBCO and/or a change in bonding nature from covalent to more ionic.

Thus, detailed structural considerations confirm the BaCuO_2 and CuO inclusions, while the question of accurately estimating the oxygen in the samples remains. Low-temperature measurements were also carried out to investigate the lattice parameters under and above the superconductivity transition (Figure 7). The results for three selected samples $x = 0.0$, 0.6 , and 1.0 reveal significant differences in the volume of unit cells depending on the Pr concentration. These relationships can be approximated by the Debye temperature formula [37]:

$$V = V_0 + I_C \frac{T^4}{\theta_D^3} \int_0^{\frac{\theta_D}{T}} \frac{x^3}{e^x - 1} dx \quad (1)$$

where V_0 is the unit cell volume at 0 K, I_C is a coefficient including the Grüneisen compressibility parameter, and θ_D is the Debye temperature.

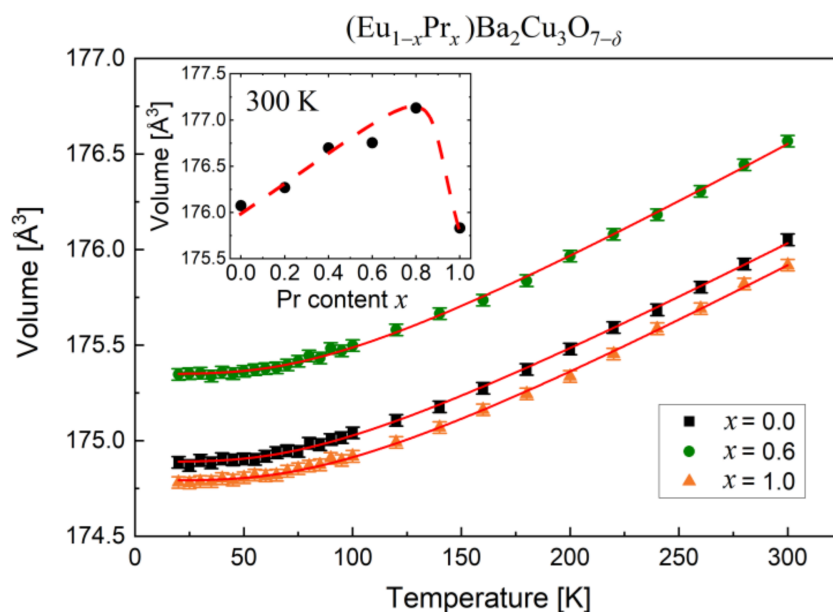


Figure 7. Unit cell volumes of selected (Eu,Pr)BCO as a function of temperature. The solid lines denote the Debye formula as described in the text. The inset shows the volumes of (Eu,Pr)BCO versus Pr content at 300 K.

In general, the unit cell volumes increase with temperature (Figure 7), as shown in Equation (1). However, above 180 K, the volumes depend almost linearly on the temperature, with I_C being the slope. The estimated parameters of Equation (1) are listed in Table 3. The inset in Figure 7 is presenting the change in unit cell volume at ambient temperature as a function of Pr concentration. This dependence clearly shows that the unit cell volume of $\text{Eu}_{0.4}\text{Pr}_{0.6}\text{BCO}$ is much larger than EuBCO or PrBCO.

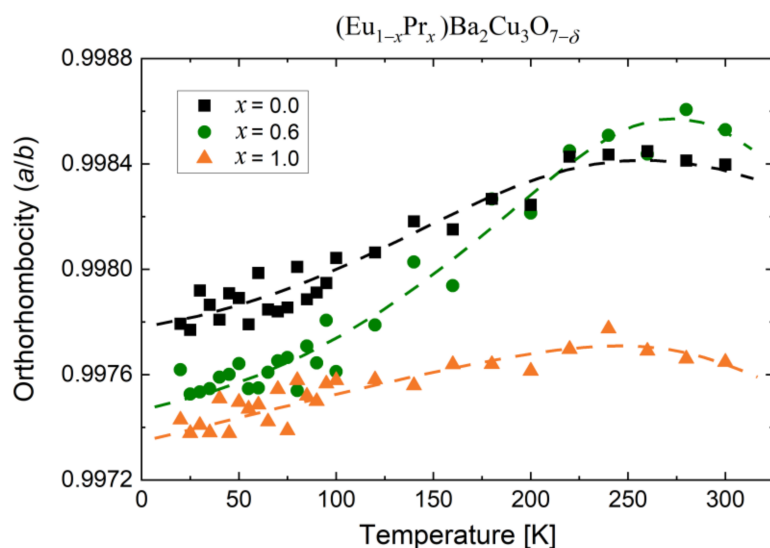
Table 3. Debye temperatures of individual (Eu,Pr)BCO.

Compound	V_o [Å ³]	θ_D [K]	I_C [Å ³ /K]
EuBCO	174.89 ± 0.04	351.5 ± 2.9	0.018 ± 0.003
(Eu _{0.4} Pr _{0.6})BCO	175.35 ± 0.04	366.1 ± 3.9	0.020 ± 0.004
PrBCO	174.79 ± 0.03	386.4 ± 3.5	0.019 ± 0.003

A significant rise in Debye temperature as the molar mass of (Eu,Pr)BCO decreases (Table 3) is evidenced by data fitting with Equation (1) and is consistent with the elastic lattice model [38]. In the literature, θ_D for EuBCO was estimated between 300 and 400 K [39], around 300 K [40], or in the range of 280 ÷ 320 K [41]. On the other hand, for YBCO doped with Pr, the Debye temperature of 350 ÷ 370 K was recorded [42]. Therefore, estimation of the θ_D parameter in this work correlates with previously reported results.

One can conclude that Pr concentration does not affect the I_C parameter, which indicates a similar nature of vibrations in the (Eu,Pr)BCO lattice. Thus, variation in the bondings, as mentioned previously, seems unlikely but still possible.

Moreover, a distinct difference in the a/b ratio was observed in the investigated temperature range (Figure 8), with no structural transitions evidenced. The a/b ratio (orthorhombicity) is a deformation measure in the basal Cu–O_{1- δ} planes; i.e., the crystallographic planes with extra O atoms adopted to $Pmmm$ structure during the air-assisted annealing process.

**Figure 8.** The $Pmmm$ unit cell deformation in the basal a/b plane versus temperature.

There is a clear tendency for the a/b ratio to increase with temperature; however, the magnitude of these changes is different. The rate of orthorhombicity change for PrBCO is slowest with temperature, while the a/b rate is slightly higher for EuBCO. The found difference indicates the high rigidity of the crystallographic structures for parent compounds. Nevertheless, the most interesting behavior is observed for Eu_{0.4}Pr_{0.6}BCO, consisting of significant growth in the a/b ratio. At low temperature, the orthorhombicity is closer to PrBCO, while above 200 K, the a/b ratio is even higher than for EuBCO. It suggests a relatively large susceptibility of the lattice constant (a) to temperature changes, in contrast to the lattice parameter (b).

3.3. Raman Spectroscopy

Two remarks on Raman-scattering spectroscopy for REBCO should be mentioned [43–45]. First, the more free charge carriers are in the material, the higher attenuation of the Raman

signal is observed. Therefore, large bandgap insulators have more pronounced phonon modes in the spectrum as compared to metals.

Second, for HTS superconductors, there is a relatively high density of carriers in the material and high absorption of visible light by the sample. Therefore, extracting the sophisticated information from Raman spectra requires low laser power densities of the excitation beam, which unfortunately provides a poor signal-to-noise ratio in the Raman spectra; however, it avoids thermal effects and specimen degradation processes.

The standard YBCO spectrum composes of three separated regions of vibrational bands [46]. Low-frequency phonon modes at $\sim 120\text{ cm}^{-1}$ and $\sim 145\text{ cm}^{-1}$ are attributed to vibrations of Ba and Cu(2) atoms, respectively. The following two bands, O(2) – O(3) (out-of-phase) and O(2) + O(3) (in-phase) [47] located around 330 cm^{-1} and 440 cm^{-1} , are directly related to the vibrations of oxygen atoms associated with conducting Cu(2)–O₂ planes.

In turn, the O(4) oxygen band detected at 500 cm^{-1} is the most reliable indicator of the YBCO superconductivity, and its position is strongly correlated to the sample heat treatment. Furthermore, the location of this peak is related to an oxygen atom referring to partially occupied Cu–O_{1- δ} planes of an insulating character, which are responsible for the oxygen deficiency in REBa₂Cu₃O_{7- δ} materials. Most importantly, for oxygen-rich REBCO ($\delta \leq 0.35$) with a well-defined *Pmmm* orthorhombic symmetry, the O(4) phonon mode is meaningfully shifted below 500 cm^{-1} , while the position of the O(4) peak above 500 cm^{-1} is characteristic for the non-superconducting *P4mm* tetragonal structure [48]. Hence, the Raman spectra of (Eu,Pr)BCO clearly show the destructive nature of the PrBCO component (Figure 9).

The most characteristic phonon mode at 500 cm^{-1} splits into two bands. The upper-frequency band O(4) shifts up to 530 cm^{-1} , whereas the lower frequency band O(4) is shifted to 485 cm^{-1} with a smaller and monotonically disappearing intensity peak compared to the 530 cm^{-1} one. It is established that the Raman frequency of the O(4) peak decreases from 500 to 485 cm^{-1} when REBCO_{7- δ} statistically loses about one oxygen atom ($\delta \approx 1$). Thus, one should expect a decrease in the oxygen stoichiometric index to a value for which (Eu,Pr)BCO_{7- δ} is no longer superconductor. For parent EuBCO and PrBCO compounds, the critical oxygen indexes were reported to be 6.5 and 6.6, respectively [49,50].

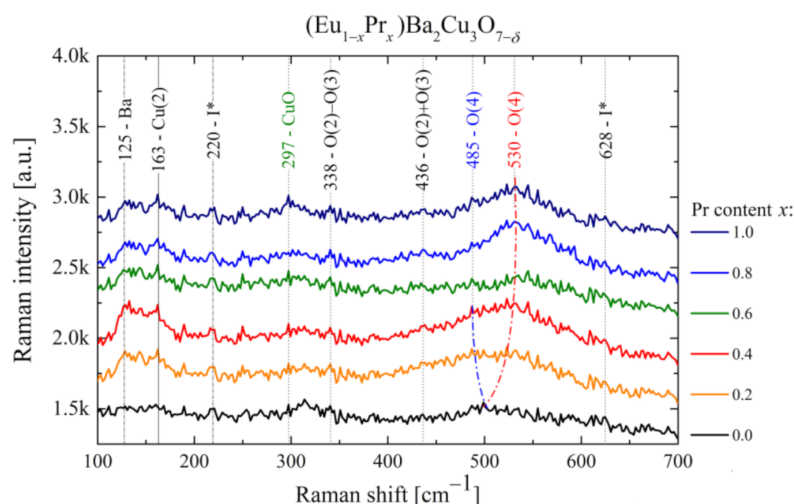


Figure 9. The Raman scattering vibrational spectra for (Eu,Pr)BCO as a function of Pr content. I* denotes the BaCuO₂ inclusions (220 cm^{-1}) and cation disorders (628 cm^{-1}), possibly indicating the structural defects in Cu–O chains [51,52].

3.4. X-ray Absorption Spectroscopy

X-ray absorption spectroscopy (XAS) is a proper in situ technique to analyze materials for the electronic structure, local bonding environments, or oxidation states. For example, Figure 10a shows the XAS spectra for the O K-edge ($1s \rightarrow 2p$).

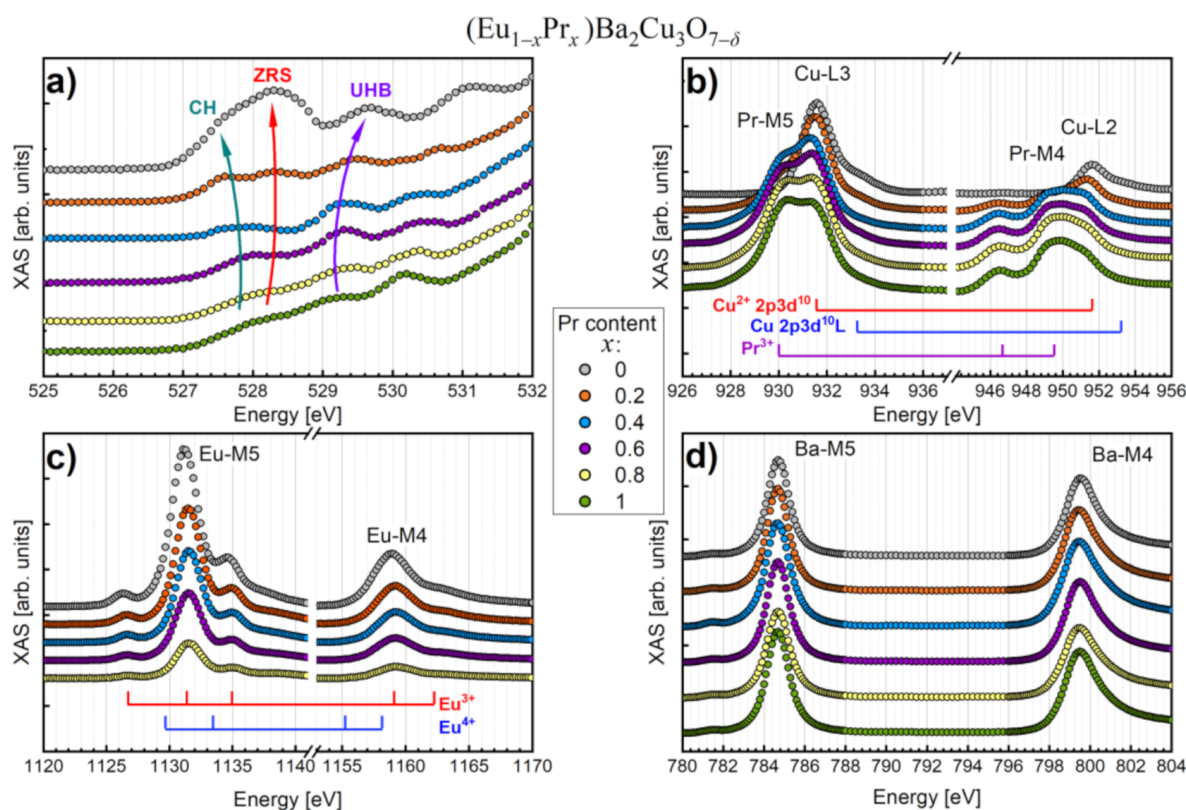


Figure 10. XAS spectra for (Eu,Pr)BCO system: (a) O K-edge, (b) Cu L2,3-edges with Pr M4,5-edges, (c) Eu M4,5-edges, and (d) Ba M4,5-edges. The valence states of Eu, Pr, and Cu, as well as the Cu–O chain holes (CH), Zhang–Rice singlets (ZRS), and upper Hubbard band (UHB) states, are marked.

Considering that the $2p$ electron levels of oxygen are hybridized with the $3d$ Cu orbitals, data inspection provides crucial information on the electric charge doping of the Cu–O₂ planes [53–57]. The XAS spectra (Figure 10a) are characterized by three significant contributions originating from the chain holes (CH) at 527.6 eV, the Zhang–Rice singlets (ZRS) of the hybridized Cu $3d_{x^2-y^2}$ and O $2p_{xy}$ orbitals within Cu–O₂ planes, as well as the upper Hubbard band (UHB) mainly related to the conduction band.

Furthermore, it is worth noting that the relative contributions of the ZRS and UHB states are related to the doping levels of the Cu–O₂ planes [53–56]. In other words, the ratio of ZRS to UHB is a straightforward indicator of the superconducting properties of cuprates. Hence, the ZRS peak is dominant for the Pr content of $x \leq 0.4$, while the UHB contribution is far more pronounced for $x > 0.4$.

Moreover, theory predicts a shift of the ZRS peak toward lower energies while moving the UHB component toward higher energies as material enters the superconducting regime [53]. The above effects were also evidenced experimentally in the $Y_{1-x}Ca_xBa_2Cu_3O_{7-\delta}$ system [56]. The CH and ZRS states must also be reflected in the Cu L-edge due to a screening effect of the so-called ligand hole (L) on the O $2p$ orbital. Since this kind of screening occurs for the square Cu–O₂ planes and straight Cu–O chains, both CH and ZRS effects should contribute to the Cu $2p3d^{10}L$ final state.

A partial overlapping with the Pr M4,5-edges complicates data analysis of the Cu L2,3-edges (Figure 10b). Nevertheless, the most relevant information can still be extracted. The final state with a hole on the ligand can be recognized as a shoulder near 933.2 eV. This anomaly is only visible for the EuBCO and Eu_{0.8}Pr_{0.2}BCO superconductors, which is consistent with the oxygen K-edge results.

In addition, the Pr M4,5-edges enable the estimation of the Pr valence state (Figure 10b). A simple distinction between 3^+ and 4^+ is due to the peak at 946.5 eV, indicating a trivalent Pr^{3+} ion in the (Eu,Pr)BCO series.

In turn, the Eu M4,5-edges lose intensity in the XAS spectrum with the Pr content (Figure 10c). The Eu/Pr substitution effect is that all spectral lines are slightly shifted toward the higher energies, and similar to Pr, the Eu ion is trivalent.

On the other hand, the Ba M4,5-edges do not show any disturbances as a function of Pr content (Figure 10d), which means no significant changes occur in the Ba sublattice. Furthermore, only a tiny pre-peak at 781.4 eV, which corresponds to the forbidden 3P_1 transition, indicates a small hybridization of the Ba $6s6p$ states with Cu $3d$ electrons.

Since the half-width at full maximum (HWHM) of the Ba M5 peaks are the same within the uncertainty levels, one may conclude that atomic mixing between the Eu/Ba and Pr/Ba sites is similar. Therefore, these results suggest that atomic disorder is not the main reason for superconductivity suppression in (Eu,Pr)BCO compounds.

3.5. Magnetization Measurements

The magnetic susceptibility curves of (Eu,Pr)BCO are shown in Figure 11a, and the hysteresis loops recorded at 5 K are presented in Figure 11b.

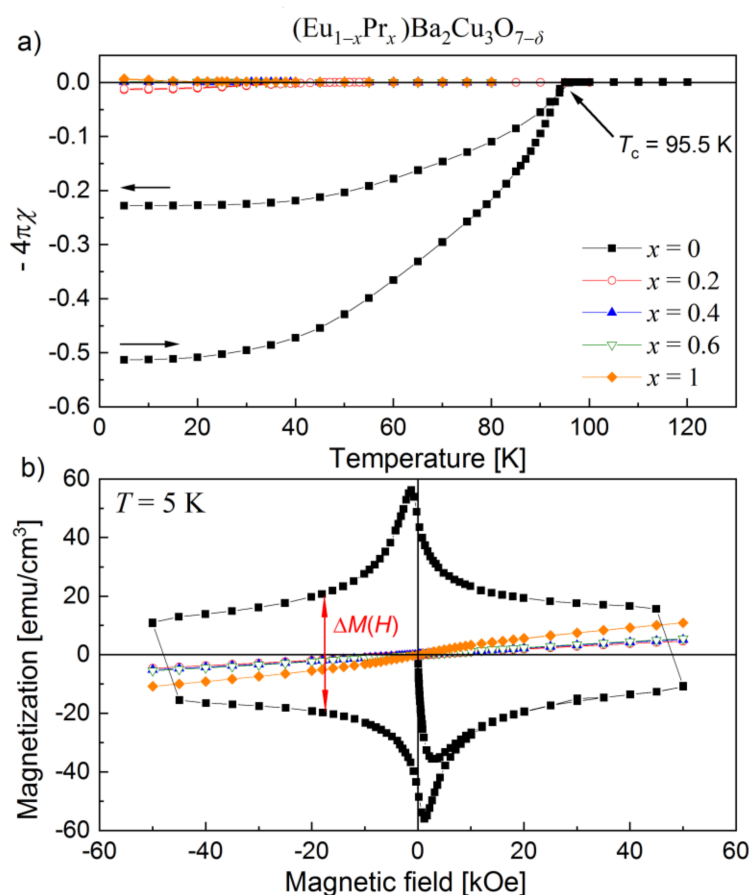


Figure 11. Magnetic curves for (Eu,Pr)BCO system: (a) DC magnetic susceptibilities, (b) hysteresis loops recorded at 5 K.

EuBCO transition from the normal state to superconductivity is seen at 95.5 K (Figure 11a). By analyzing the magnetization data as $-4\pi\chi(T)$, one can see how drastically the Pr atoms incorporated into the (Eu,Pr)BCO system reduce the Meissner effect. For Eu_{0.8}Pr_{0.2}BCO, the critical temperature (T_c) is lowered twice to 45 K.

In addition, the complete disappearance of thermal hysteresis of the $M(T)$ curves (Figure 11a) suggests a strong suppression of the superconducting properties induced by praseodymium. A related effect is also seen in Figure 11b, where there is a broad hysteresis loop for EuBCO, which is characteristic of superconductors. At the same time, for (Eu,Pr)BCO compounds, almost the straight $M(H)$ lines typical for paramagnetic or antiferromagnetic materials are detected.

For $x \geq 0.4$, the superconducting state is completely lost (positive χ in Figure 11a), which is not surprising, since many (RE,Pr)BCO compounds exhibit a Pr-induced suppression of the superconductivity [58–71].

Using the Bean critical-state model [72–74], it is possible to estimate the superconducting critical current density (J_c) of (Eu,Pr)BCO according to the formula:

$$J_c(H) = \frac{20 \cdot \Delta M(H)}{a \cdot \left(1 - \frac{a}{3b}\right)} \quad (2)$$

where a and b are the sample dimensions perpendicular to the applied magnetic field, and ΔM is a difference in magnetizations $M_{\downarrow} - M_{\uparrow}$ when sweeping the H field down and up, respectively.

As mentioned above, estimating the critical current density only becomes meaningful for EuBCO and $\text{Eu}_{0.8}\text{Pr}_{0.2}\text{BCO}$. A significant J_c attenuation from two to three orders of magnitude for $\text{Eu}_{0.8}\text{Pr}_{0.2}\text{BCO}$ is shown in Figure 12. There is also a slight loss of J_c along the internal magnetic field, confirming its destructive nature for the superconducting state.

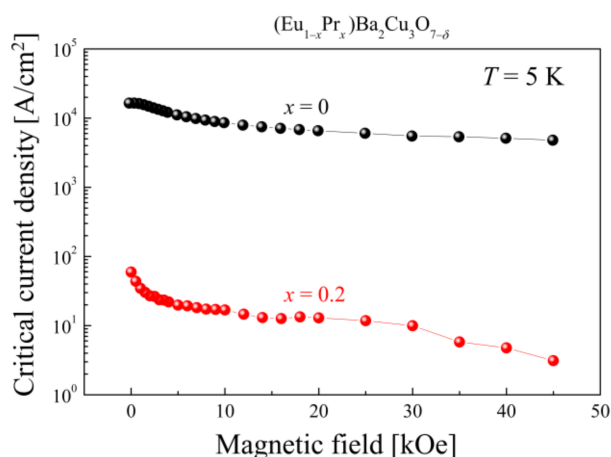


Figure 12. Critical current densities for EuBCO and $\text{Eu}_{0.8}\text{Pr}_{0.2}\text{BCO}$ as a function of the magnetic field.

3.6. Oxygen Index

The collected results consistently describe the properties of (Eu,Pr)BCO except for $\text{Eu}_{0.6}\text{Pr}_{0.4}\text{BCO}$, where the structural and spectroscopic measurements concerning magnetic studies exhibit some discrepancies. Furthermore, the $\text{Eu}_{0.6}\text{Pr}_{0.4}\text{BCO}$ material is controversial as to the nature of conductivity, as not all investigation methods indicate its superconductivity state. Therefore, it was decided to resolve this uncertainty by determining the oxygen index by the iodometric titration method.

The results are presented in Figure 13, where the gradual loss of oxygen in the $Pnmm$ structure is visible. This phenomenon slowly progresses up to $\text{Eu}_{0.6}\text{Pr}_{0.4}\text{BCO}$; then, a rapid decrease in the oxygen content ($\Delta n = 0.24$) is observed. The same rule applies to a further increase in the Pr content. The $\text{Eu}_{0.4}\text{Pr}_{0.6}\text{BCO}$ and $\text{Eu}_{0.2}\text{Pr}_{0.8}\text{BCO}$ samples show a similar O concentration, while PrBCO exhibits a further oxygen loss of $\Delta n = 0.38$.

The above observations allowed the discrimination of three areas of different conductivity types. First, the most oxygenated samples up to $x = 0.4$ are characterized by the superconductivity state at low temperatures.

Second, samples with a higher Pr content lose their superconducting properties at a macro scale, passing into the ohmic conduction mechanism. However, this behavior does not exclude a mixed (vortex) state with small intragranular superconductivity and dominant ohmic conductivity. In contrast, PrBCO does not possess any superconducting properties at all.

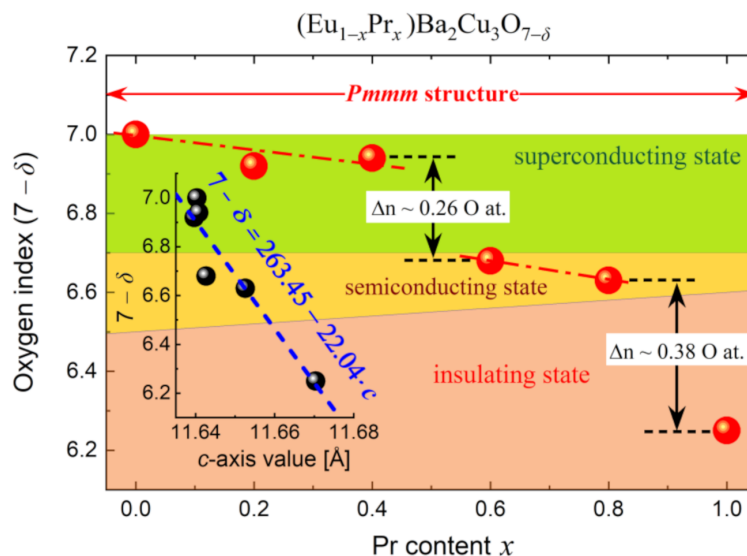


Figure 13. Schematic diagram of the conductivity regions for (Eu,Pr)BCO as a function of Pr content and c -axis value of $Pmmm$ orthorhombic unit cell (inset).

Similar conclusions can be drawn from the dependence of the c lattice parameter on the oxygen index $7-\delta$ (inset in Figure 13). Considering a strong negative correlation due to relation $7-\delta = 263.45 - 22.04 \cdot c$, the higher Pr content elongates the size of the unit cell in the $[001]$ direction, which makes the $Pmmm$ structure easier to adopt oxygen atoms in the $\text{Cu}-\text{O}_2$ planes (reduction of holes) than in the metallic $\text{Cu}-\text{O}_{1-\delta}$ layers responsible for the superconductivity state of the REBCO materials.

4. Summary

A solid-state reaction method was proven to be an effective procedure for synthesizing the (Eu,Pr)BCO materials. The sinters are characterized by dense, compact microstructures with slight inclusions of BaCuO_2 and CuO .

According to XRD data, the orthorhombic $Pmmm$ structure was the dominant phase for all (Eu,Pr)BCO. Furthermore, low-temperature XRD studies evidenced that phononic properties depend on the molar mass of Eu and Pr (strong dependence of the Debye temperature), while the actual lattice volume is a secondary factor.

For conventional superconductors, a linear electron–phonon coupling is the foundation of the BCS theory [75]. In this formalism, Debye temperature (θ_D) growth means enhancing the electron–phonon coupling parameter (λ) due to the increase of phononic frequencies, which is reflected in the so-called isotopic effect.

However, for HTS materials, the role of electron–phonon interaction is not straightforward. Commonly, no isotopic effect is observed, which is often incorrectly attributed to a lack of electron–phonon coupling. In fact, the electron–phonon coupling in cuprates is much stronger and nonlinear than in conventional superconductors [76]. Therefore, for HTS materials, the electronic structure and lattice dynamics are crucial for discussing superconductivity suppression.

For cuprates, acoustic and optical phonons related to $\text{Cu}-\text{O}$ bonds in- and out-of-plane are essential to establish the electron–phonon coupling [75,76]. Moreover, the acoustic phonons energies are enhanced for PrBCO compared to EuBCO, as evidenced by the rising

Debye temperature. For this reason, it should be concluded that the electronic properties of (Eu,Pr)BCO and optical phonons are mainly responsible for HTS state suppression.

Indeed, XAS and Raman spectroscopies clearly showed a gradual deterioration of HTS state with Pr content driven by hole depletion of the Cu–O₂ planes. The stretching mode Cu(1)–O(4) along the *c*-axis (500 cm^{−1}) is known to be sensitive to oxygen content, and the lower oxygen concentration in the superconducting phase is expected to redshift this peak. However, the increase of praseodymium in the (Eu,Pr)BCO system splits a 500 cm^{−1} band into two lines, which is characteristic for the superconductivity state (485 cm^{−1}) and ohmic conductivity (530 cm^{−1}). This behavior reliably describes the gradual disappearance of the HTS state by suppressing the intragranular scale superconductivity for *x* > 0.4 due to insufficient oxygen factor.

On the other hand, XAS showed that for *x* > 0.4, the Cu 2*p*3*d*¹⁰L final state indicating high mobility of holes in the Cu–O₂ planes is absent. Therefore, the depletion of the carriers and their localization is a leading mechanism of HTS loss in Eu_{1−*x*}Pr_{*x*}BCO. The above discussion is summarized in the form of a schematic diagram presented in Figure 13.

Author Contributions: Conceptualization, P.P.; methodology, P.P.; validation, P.P.; formal analysis, P.P.; investigation, P.P., C.J., J.P., E.D. and Ł.G.; resources, P.P.; writing—original draft preparation, P.P.; writing—review and editing, P.P., P.Z., C.J., J.P., E.D. and Ł.G.; visualization, P.P., P.Z., E.D. and Ł.G.; supervision, P.P. and Ł.G.; project administration, P.P. All authors have read and agreed to the published version of the manuscript.

Funding: This research received no external funding.

Institutional Review Board Statement: Not applicable.

Informed Consent Statement: Not applicable.

Data Availability Statement: The data presented in this study are available on request from the corresponding author.

Acknowledgments: The authors would like to express their deepest gratitude to the PEEM/XAS end-line operators at the SOLARIS National Synchrotron Radiation Center in Kraków (Poland), Marcin Zając and Joanna Stępień, as well as Agata Kamińska from Cardinal Stefan Wyszyński University and Marcin Kowalik from AGH University of Science and Technology for their help during the experiment. The authors are also grateful to Magdalena Parlińska-Wojtan from the Institute of Nuclear Physics PAS for SEM/EDS analysis. Furthermore, the Laboratory for Structural and Biochemical Research of the University of Warsaw has supported the iodometric titration method. Finally, the authors would like to thank Andrzej Veitia from PsiQuantum, Palo Alto, CA, USA, for reading and re-vising this manuscript.

Conflicts of Interest: The authors declare no conflict of interest. The funders had no role in the research design, data collection, analyses, interpretation, writing the manuscript, or publishing the results.

References

1. Bednorz, J.G.; Müller, K.A. Possible high *T_c* superconductivity in the Ba–La–Cu–O system. *Z. Phys. B* **1986**, *64*, 189–193. [[CrossRef](#)]
2. Chu, C.W.; Hor, P.H.; Meng, R.L.; Gao, I.; Huang, Z.J.; Wang, Y.Q. Evidence for superconductivity above 40 K in the La–Ba–Cu–O compound system. *Phys. Rev. Lett.* **1987**, *58*, 405–407. [[CrossRef](#)] [[PubMed](#)]
3. Wu, M.K.; Ashburn, J.R.; Torng, C.J.; Hor, P.H.; Meng, R.L.; Gao, L.; Huang, Z.J.; Wang, Y.Q.; Chu, C.W. Superconductivity at 93 K in a new mixed-phase Y–Ba–Cu–O compound system at ambient pressure. *Phys. Rev. Lett.* **1987**, *58*, 908–910. [[CrossRef](#)] [[PubMed](#)]
4. Maple, M.B.; Dalichaouch, Y.; Ferreira, J.M.; Hake, R.R.; Lee, B.W.; Neumeier, J.J.; Torikachvili, M.S.; Yang, K.N.; Zhou, H.; Guertin, R.P.; et al. RBa₂Cu₃O_{7−*δ*} (*R* = rare earth) high-*T_c* magnetic superconductors. *Phys. B C* **1987**, *148*, 155–162. [[CrossRef](#)]
5. Yang, H.C.; Hsieh, M.H.; Sung, H.H.; Chen, C.H.; Horng, H.E.; Kan, Y.S.; Chen, H.C.; Jao, J.C. High-temperature resistivity of RBa₂Cu₃O_{7−*x*}, where *R* = La, Pr, Nd, Sm, Eu, Dy, Ho, Er and Tm. *Phys. Rev. B* **1989**, *39*, 9203–9208. [[CrossRef](#)]
6. Jin, S.J.; Fastnacht, R.A.; Tiefel, T.H.; Sherwood, R.C. Transport critical current in rare-earth-substituted superconductors RBa₂Cu₃O_{7−*δ*} (*R* = Gd, Dy, Sm, Ho, Y). *Phys. Rev. B* **1988**, *37*, 5828–5830. [[CrossRef](#)]
7. Kumar-Naik, S.P.; Bai, V.S. The effect of resolidification on preform optimized infiltration growth processed (Y, Nd, Sm, Gd) B.C.O., multi-grain bulk superconductor. *Cryogenics* **2017**, *81*, 47–53. [[CrossRef](#)]

8. Pęczkowski, P.; Kowalik, M.; Zachariasz, P.; Jastrzębski, C.; Jaegermann, Z.; Szterner, P.; Woch, W.M.; Szczytko, J. Synthesis and physicochemical properties of Nd-, Sm-, Eu-based cuprate high-temperature superconductors. *Phys. Stat. Soli. A* **2018**, *215*, 170088. [[CrossRef](#)]
9. Pęczkowski, P.; Szterner, P.; Jaegermann, Z.; Kowalik, M.; Zalecki, R.; Woch, W.M. Effect of forming pressure on physicochemical properties of YBCO ceramics. *J. Supercond. Nov. Magn.* **2018**, *31*, 2719–2732. [[CrossRef](#)]
10. Engler, E.M.; Lee, Y.Y.; Nazzal, A.I.; Beyers, R.B.; Lim, G.; Grant, P.M.; Parkin, S.S.P.; Ramirez, M.L.; Vazquez, J.E.; Savoy, R.J. Superconductivity above liquid nitrogen temperature: Preparation and properties of a family of perovskite-based superconductors. *J. Am. Chem. Soc. Commun.* **1987**, *109*, 2848–2849. [[CrossRef](#)]
11. Hor, P.H.; Meng, R.L.; Wang, Y.Q.; Gao, L.; Huang, Z.L.; Bechtold, J.; Forster, K.; Chu, C.W. Superconductivity above 90 K in the square-planar compound system $ABa_2Cu_3O_{6+x}$ with $A = Y, La, Nd, Sm, Eu, Gd, Ho, Er$ and Lu . *Phys. Rev. Lett.* **1987**, *58*, 1891–1894. [[CrossRef](#)]
12. Chu, C.W. Dimensionality of high temperature superconductivity in oxides. In *Physics of Low-Dimensional System, Proceedings of Nobel Symposium 73*; Lundqvist, S., Nilsson, N.R., Eds.; Co-Published with World Scientific: Gräntåvallen, Sweden, 1989; pp. 11–18.
13. López-Morales, M.E.; Ríos-Jara, D.; Tagüeña, J.; Escudero, R.; La Placa, S.; Bezingue, A.; Lee, V.Y.; Engler, E.M.; Grant, P.M. Role of oxygen in $PrBa_2Cu_3O_{7-y}$: Effect on structural and physical properties. *Phys. Rev. B* **1990**, *41*, 6655–6667. [[CrossRef](#)]
14. López-Morales, M.E.; Ríos-Jara, D.; Tagüeña-Martinez, J.; Escudero, R.; Gomez-Lara, J. On the crystallographic structure and electronic behaviour of $Pr_1Ba_2Cu_3O_y$. *Phys. C* **1988**, *153–155*, 942–943. [[CrossRef](#)]
15. Blackstead, H.A.; Dow, J.D. Implications of superconductivity of $PrBa_2Cu_3O_7$. *Sol. Stat. Commun.* **2000**, *115*, 137–140. [[CrossRef](#)]
16. Blackstead, H.A.; Chrisey, D.B.; Dow, J.D.; Horwitz, J.S.; Klunzinger, A.E.; Pulling, D.B. Superconductivity in $PrBa_2Cu_3O_7$. *Phys. Lett. A* **1995**, *207*, 109–112. [[CrossRef](#)]
17. Usagawa, T.; Ishimaru, Y.; Wen, J.; Utagawa, T.; Koyama, S.; Enomoto, Y. Superconductivity in (110) $PrBa_2Cu_3O_{7-\delta}$ thin films pseudomorphically grown on (110) $YBa_2Cu_3O_{7-\delta}$ single crystal substrates. *Jap. J. App. Phys.* **1997**, *36*, L1583. [[CrossRef](#)]
18. Łuszczek, M.; Sadowski, W. Surface morphology of $PrBa_2Cu_3O_{7-\delta}$ single crystals after the long-lasting high-temperature reduction. *Open Phys.* **2003**, *1*, 626–633. [[CrossRef](#)]
19. Łuszczek, M.; Sadowski, W.; Klimczuk, T.; Olchowik, J.; Susla, B.; Czajka, B. Superconductivity in $PrBa_2Cu_3O_7$ single crystals after high-temperature thermal treatment. *Phys. C* **1999**, *322*, 57–64. [[CrossRef](#)]
20. Zou, Z.; Oka, K.; Ito, T.; Nishihara, N. Bulk superconductivity in single crystals of $PrBa_2Cu_3O_x$. *Jap. J. App. Phys.* **1997**, *36*, L18–L20. [[CrossRef](#)]
21. Hults, W.L.; Cooley, J.C.; Peterson, E.J.; Smith, J.L.; Blackstead, H.A.; Dow, J.D. $PrBa_2Cu_3O_x$ polycrystalline superconductor preparation. *Int. J. Mod. Phys. B* **1998**, *12*, 3278–3283. [[CrossRef](#)]
22. Barros, F.M.; Pureur, P.; Schaf, J.; Fabris, F.W.; Vieira, V.N.; Jurelo, A.R.; Cantao, M.P. Unconventional superconducting granularity of the $Y_{1-x}Pr_xBa_2Cu_3O_{7-\delta}$ compound. *Phys. Rev. B* **2006**, *73*, 094515. [[CrossRef](#)]
23. Soderholm, L.; Zhang, K.; Hinks, D.G.; Beno, M.A.; Jorgensen, J.D.; Segre, C.U.; Schuller, I.K. Incorporation of Pr in $YBa_2Cu_3O_{7-\delta}$: Electronic effects on superconductivity. *Nature* **1987**, *328*, 604–605. [[CrossRef](#)]
24. Jee, C.-S.; Kebede, A.; Nichols, D.; Crow, J.E.; Mihalissin, T.; Myer, G.H.; Perez, I.; Salomon, R.E.; Schlottmann, P. Depression of superconductivity, heavy fermion behavior and valence fluctuations in $Y_{1-x}Pr_xBa_2Cu_3O_7$. *Soli. Stat. Comm.* **1989**, *69*, 379–384. [[CrossRef](#)]
25. Das, I.; Sampathkumaran, E.V.; Vijayaraghavan, R. Magnetic and superconducting behavior of the oxides, $Pr_{1-x}Gd_xBa_2Cu_3O_y$. *Phys. C Supercond.* **1991**, *173*, 331–336. [[CrossRef](#)]
26. Pęczkowski, P.; Zachariasz, P.; Kowalik, M.; Zalecki, R.; Jastrzębski, C. Characterization of the superconductor-multiferroic type materials based on $YBa_2Cu_3O_{7-\delta}$ - $YMnO_3$ composites. *Ceram. Internat.* **2019**, *45*, 18189–18204. [[CrossRef](#)]
27. Kramer, M.J.; Yoo, S.I.; McCallum, R.W.; Yelon, W.B.; Xie, H.; Allenspach, P. Hole filling charge transfer and superconductivity in $Nd_{1+x}Ba_{2-x}Cu_3O_{7+\delta}$. *Phys. C* **1994**, *219*, 145–155. [[CrossRef](#)]
28. Łatka, K. Investigation of the praseodymium role in superconductivity of $(Eu_{1-x}Pr_x)Ba_2Cu_3O_{7-\delta}$ and related compounds. *Phys. C Supercond.* **1990**, *171*, 287–292. [[CrossRef](#)]
29. Nieva, G.; Ghamaty, G.; Lee, B.W.; Maple, M.B.; Schuller, I.K. Superconductivity and magnetism in $Eu_{1-x}Pr_xBa_2Cu_3O_{7-\delta}$. *Phys. Rev. B* **1991**, *44*, 6999–7007. [[CrossRef](#)]
30. Alagöz, S. production of YBCO superconductor sample by powder-in-tube method (PITM); and effect of Cd and Ga doping on the system. *Turkish J. Phys.* **2009**, *33*, 69–80.
31. Rietveld, H.M. Line profiles of neutron powder-diffraction peaks for structure refinement. *Acta Crystallogr.* **1967**, *22*, 151–152. [[CrossRef](#)]
32. Rodriguez-Carvajal, J. Recent advances in magnetic structure determination by neutron powder diffraction. *Phys. B* **1993**, *192*, 55–69. [[CrossRef](#)]
33. Karppinen, M.; Niinistö, L. Determination of the oxygen content in the superconducting $YBa_2Cu_3O_{7-\delta}$ phase. *Supercond. Sci. Tech.* **1991**, *4*, 334–336. [[CrossRef](#)]
34. Seitz, M.; Oliver, A.G.; Raymond, K.N. The lanthanide contraction revisited. *J. Am. Chem. Soc.* **2007**, *129*, 11153–11160. [[CrossRef](#)]
35. Quadrelli, E.A. Lanthanide contraction over the 4f series follows a quadratic decay. *Inorg. Chem.* **2002**, *41*, 167–169. [[CrossRef](#)]
36. Benzi, P.; Bottizzo, E.; Rizzi, N. Oxygen determination from cell dimensions in YBCO superconductors. *J. Cryst. Growth* **2004**, *269*, 625–629. [[CrossRef](#)]

37. Sayetat, F.; Fertey, P.; Kessler, M. An easy method for the determination of Debye temperature from thermal expansion analyses. *J. App. Crystallogr.* **1998**, *31*, 121–127. [[CrossRef](#)]
38. Prasher, R.; Tong, T.; Majumdar, A. An acoustic and dimensional mismatch model for thermal boundary conductance between a vertical mesoscopic nanowire/nanotube and a bulk substrate. *J. App. Phys.* **2007**, *102*, 104312. [[CrossRef](#)]
39. Capaccioli, M.; Cianchi, L.; Giallo, F.D.; Oieralli, F.; Spina, G. Low-temperature vibrational anharmonicity of ^{151}Eu in $\text{EuBa}_2\text{Cu}_3\text{O}_{7-\delta}$. *J. Phys. Condens. Matter* **1995**, *7*, 2429–2438. [[CrossRef](#)]
40. Wortmann, G.; Blumenröder, S.; Freimuth, A.; Riegel, D. ^{151}Eu -Mössbauer study of the high- T_c superconductor $\text{EuBa}_2\text{Cu}_3\text{O}_{7-x}$. *Phys. Lett. A* **1988**, *126*, 434–438. [[CrossRef](#)]
41. Graczyk, P.; Krawczyk, M.; Dhuey, S.; Yang, W.-G.; Schmidt, H.; Gubbiotti, G. Magnonic band gap and mode hybridization in continuous permalloy films induced by vertical dynamic coupling with an array of permalloy ellipses. *Phys. Rev. B* **2018**, *98*, 174420. [[CrossRef](#)]
42. Khadzhai, G.Y.; Vovk, N.R.; Vovk, R.V. Conductivity of single-crystal $\text{Y}_{1-y}\text{Pr}_y\text{Ba}_2\text{Cu}_3\text{O}_{7-\delta}$ over a wide range of temperatures and Pr concentrations. *Low Temp. Phys.* **2014**, *40*, 488–491. [[CrossRef](#)]
43. Galinetto, P.; Malavasi, L.; Flor, G. Structural investigation of high- T_c superconductor $\text{EuBa}_2\text{Cu}_3\text{O}_y$ by microRaman spectroscopy. *Soli. Stat. Commun.* **2001**, *119*, 33–38. [[CrossRef](#)]
44. Georgieva, S.; Stoyanova-Ivanova, A.; Abrashev, M. Estimation of the oxygen content of $\text{RBa}_2\text{Cu}_3\text{O}_y$ (R = Er, Y, Eu, Dy) superconducting samples by spectrophotometry and Raman spectroscopy: A comparison between chemical and physical methods for oxygen determination. *Mediterr. J. Phys.* **2016**, *1*, 16–21.
45. Tavana, A.; Khosroabadi, H.; Akhavan, M. Phonon frequency calculations of GdBCO and PrBCO. *Phys. Stat. Soli. C* **2006**, *3*, 3162–3165. [[CrossRef](#)]
46. Maroni, V.A.; Reeves, J.L.; Schwab, G. On-line characterization of YBCO coated conductors using Raman spectroscopy methods. *App. Spect.* **2007**, *61*, 359–366. [[CrossRef](#)]
47. Wang, S.-S.; Li, F.; Wu, H.; Zhang, Y.; Muhammad, S.; Zhao, P.; Le, X.-Y.; Xiao, Z.-S.; Jiang, L.-X.; Ou, X.-D.; et al. Low-energy (40 keV) proton irradiation of $\text{YBa}_2\text{Cu}_3\text{O}_{7-x}$ thin films: Micro-Raman characterization and electrical transport properties. *Chin. Phys. B* **2019**, *28*, 027401. [[CrossRef](#)]
48. Ambrosch-Draxl, C.; Auer, H.; Kouba, R.; Sherman, E.Y. Raman scattering in $\text{YBa}_2\text{Cu}_3\text{O}_7$: A comprehensive theoretical study in comparison with experiments. *Phys. Rev. B* **2002**, *65*, 064501. [[CrossRef](#)]
49. Przybylo, W.; Fitzner, K. The oxygen stoichiometry of the $\text{EuBa}_2\text{Cu}_3\text{O}_{7-x}$ phase investigated by thermogravimetry. *Mat. Res. Bull.* **1995**, *30*, 1413–1419. [[CrossRef](#)]
50. Radousky, H.B. A review of the superconducting and normal state properties of $\text{Y}_{1-x}\text{Pr}_x\text{Ba}_2\text{Cu}_3\text{O}_7$. *J. Mater. Res.* **1992**, *7*, 1917–1955. [[CrossRef](#)]
51. Martinho, H.; Martin, A.A.; Rettori, C.; Lin, C.T. Origin of the A_{1g} and B_{1g} electronic Raman scattering peaks in the superconducting state of $\text{YBa}_2\text{Cu}_3\text{O}_7$. *Phys. Rev. B* **2004**, *69*, 180501. [[CrossRef](#)]
52. Gibson, G.; Cohen, L.F.; Humphreys, R.G.; MacManus-Driscoll, J. A Raman measurement of cation disorder in $\text{YBa}_2\text{Cu}_3\text{O}_{7-x}$ thin films. *Phys. C Supercond.* **2000**, *333*, 139–145. [[CrossRef](#)]
53. Chen, C.-C.; Sentef, M.; Kung, Y.F.; Jia, C.J.; Thomale, R.; Moritz, B.; Kampf, A.P.; Devereaux, T.P. Doping evolution of the oxygen K-edge X-ray absorption spectra of cuprate superconductors using a three-orbital Hubbard model. *Phys. Rev. B* **2013**, *87*, 165144. [[CrossRef](#)]
54. Zhang, F.C.; Rice, T.M. Effective Hamiltonian for the superconducting Cu oxides. *Phys. Rev. B* **1988**, *37*, 3759–3761. [[CrossRef](#)]
55. Chen, C.T.; Sette, F.; Ma, Y.; Hybertsen, M.S.; Stechel, E.B.; Foulkes, W.M.C.; Schuller, M.; Cheong, S.-W.; Cooper, A.S.; Rupp, L.W., Jr.; et al. Electronic states in $\text{La}_{2-x}\text{Sr}_x\text{CuO}_{4+\delta}$ probed by soft-X-ray absorption. *Phys. Rev. Lett.* **1991**, *66*, 104–107. [[CrossRef](#)]
56. Chen, Y.-J.; Jiang, M.G.; Luo, C.W.; Lin, J.-Y.; Wu, K.H.; Lee, J.M.; Chen, J.M.; Kuo, Y.K.; Juang, J.Y.; Mou, C.-Y. Doping evolution of Zhang-Rice singlet spectral weight: A comprehensive examination by X-ray absorption spectroscopy. *Phys. Rev. B* **2013**, *88*, 134525. [[CrossRef](#)]
57. Salluzzo, M.; Ghiringhelli, G.; Brookes, N.B.; De Luca, G.M.; Fracassi, F.; Vaglio, R. Superconducting-insulator transition driven by out-of-plane carrier localization in $\text{Nd}_{1.2}\text{Ba}_{1.8}\text{Cu}_3\text{O}_{7+x}$ ultrathin films. *Phys. Rev. B* **2007**, *75*, 054519. [[CrossRef](#)]
58. Zhuo, Y.; Choi, J.-H.; Kim, M.-S.; Park, J.-N.; Bae, M.-K.; Lee, S.-I. Effects of Pr ion on the superconducting properties in $\text{Y}_{1-x}\text{Pr}_x\text{Ba}_2\text{Cu}_3\text{O}_{7-\delta}$ single crystals. *Phys. Rev. B* **1997**, *56*, 8381–8385. [[CrossRef](#)]
59. Doyle, B.N.; Shah, S.N. Study of $\text{Pr}_x\text{Y}_{1-x}\text{Ba}_2\text{Cu}_3\text{O}_{7-\delta}$ high T_c superconductors. *Indian J. Pur. App. Phys.* **2005**, *43*, 279–286.
60. Palles, D.; Lampakis, D.; Siranidi, E.; Liarokapis, E.; Gantis, A.; Calamitidou, M. Texture, strains, and superconductivity in $\text{Y}_{1-x}\text{Pr}_x\text{Ba}_2\text{Cu}_3\text{O}_{7-\delta}$. *Phys. C* **2007**, *460–462*, 922–924. [[CrossRef](#)]
61. Yu, J.; Zhao, Y.; Zhang, H. Dramatic increase of paramagnetism before superconductivity quenches in $\text{Y}_{1-x}\text{Pr}_x\text{Ba}_2\text{Cu}_3\text{O}_{7-\delta}$. *Phys. C* **2008**, *468*, 1198–1201. [[CrossRef](#)]
62. Lin, J.G.; Xue, Y.Y.; Chu, C.W.; Cao, X.W.; Ho, J.C. Pressure effect on the superconducting transition temperature of $\text{Dy}_{1-x}\text{Pr}_x\text{Ba}_2\text{Cu}_3\text{O}_{7-\delta}$. *J. App. Phys.* **1993**, *73*, 5871–5873. [[CrossRef](#)]
63. Khosroabadi, H.; Daadmehr, V.; Akhavan, M. Magnetic transport properties and Hall effect in $\text{Gd}_{1-x}\text{Pr}_x\text{Ba}_2\text{Cu}_3\text{O}_{7-\delta}$ system. *Phys. C* **2003**, *384*, 169–177. [[CrossRef](#)]

64. Awana, V.P.S.; Dou, S.X.; Singh, R.; Narlikar, A.V.; Malik, S.K.; Yelon, W.B. Magnetic and superconducting properties of Pr in $\text{La}_{1-x}\text{Pr}_x\text{BaCaCu}_3\text{O}_7$ system with $0.0 \leq x \leq 1.0$. *J. App. Phys.* **1998**, *83*, 7315–7317. [[CrossRef](#)]
65. Murugesan, M.; Ishigaki, T.; Kuwano, H.; Chen, M.; Liu, R.S.; Nachimuthu, P. Enhancement of critical Pr ion concentration (X_{Cr}) in $(\text{La}_{1-x}\text{Pr}_x)\text{Ba}_2\text{Cu}_3\text{O}_z$. *J. App. Phys.* **1999**, *86*, 6985–6992. [[CrossRef](#)]
66. Luo, H.M.; Ding, S.Y.; Wu, X.S. Coexistence of superconductivity and antiferromagnetism in the $\text{La}_{1-x}\text{Pr}_x\text{Ba}_2\text{Cu}_3\text{O}_7$ system. *J. App. Phys.* **2001**, *89*, 7663–7665. [[CrossRef](#)]
67. Zhang, C.; Zhang, Y. Crystallographic evolution and superconductivity in the $\text{La}_{1.85-x}\text{Pr}_x\text{Sr}_{0.15}\text{CuO}_4$ system ($0 \leq x \leq 1.85$). *J. Phys. Cond. Matt.* **2002**, *14*, 7383–7389. [[CrossRef](#)]
68. Cao, X.W.; Tang, Y.J.; Ho, J.C. Superconducting T_c and normal-state resistivity in $\text{Nd}_{1-x}\text{Pr}_x\text{Ba}_2\text{Cu}_3\text{O}_{7-\delta}$ system. *Phys. C* **1996**, *259*, 361–364. [[CrossRef](#)]
69. Awana, V.P.S.; Cardoso, C.A.; de Lima, O.F.; Singh, R.; Narlikar, A.V.; Yelon, W.B.; Malik, S.K. Suppression of superconductivity with Pr substitution in $\text{Nd}_{1-x}\text{Pr}_x\text{BaCaCu}_3\text{O}_7$ system. *Phys. C* **1999**, *316*, 113–118. [[CrossRef](#)]
70. Tomkowicz, Z. Trapping mechanism of superconductivity suppression induced by Pr substitution in the $\text{Ho}_{1-x}\text{Pr}_x\text{Ba}_2\text{Cu}_3\text{O}_{7-\delta}$ system. *Phys. C* **1999**, *320*, 173–182. [[CrossRef](#)]
71. Tomkowicz, Z.; Bałanda, M.; Zaleski, A.J. AC and DC magnetic studies of critical currents in ceramics of the $\text{Ho}_{1-x}\text{Pr}_x\text{Ba}_2\text{Cu}_3\text{O}_{7-\delta}$ system. *Phys. C* **2002**, *370*, 259–268. [[CrossRef](#)]
72. Gyorgy, E.M.; van Dover, R.B.; Jackson, K.A.; Schneemeyer, L.F.; Waszczak, J.V. Anisotropic critical currents in $\text{Ba}_2\text{YCu}_3\text{O}_7$ analyzed using an extended Bean model. *Appl. Phys. Lett.* **1989**, *55*, 283–285. [[CrossRef](#)]
73. Bean, C.P. Magnetization of hard superconductors. *Phys. Rev. Lett.* **1962**, *8*, 250–253. [[CrossRef](#)]
74. Bean, C.P. Magnetization of high-field superconductors. *Rev. Mod. Phys.* **1964**, *36*, 31–39. [[CrossRef](#)]
75. Mourachkine, A. *High-Temperature Superconductivity in Cuprates; The Nonlinear Mechanism and Tunneling Measurements*; Springer: Dordrecht, The Netherlands, 2002.
76. Kulić, M.L. Interplay of electron-phonon interaction and strong correlations: The possible way to high-temperature superconductivity. *Phys. Rep.* **2000**, *338*, 1–264. [[CrossRef](#)]